

Studies of Fabric Permeability

The following summarises the findings of a collaborative project on “Engineering the performance and functional properties of technical textiles”. The other partners of the project were: Heriot –Watt University and UMIST (now part of Manchester University). The aspect of the work reported here concerns the “Fluid Flow and Vapour Diffusion Measurement and Modelling of Technical Textiles”

Grant Awarding Body: EPSRC

Research Team:

C.A. Lawrence (Principal Investigator)

M. P.U. Bandara (Co-investigator)

D. Brooke (Co-investigator)

S. J. Russell (Co-investigator)

M.R. Mahmoudi (Research Fellow)

M.R. Taylor (Research Fellow)

K. White (Engineering Technician)

Methodology:

The work was undertaken in three parts:

- The construction and evaluation of a novel instrument for measuring air permeability characteristics of fabrics at differential pressure levels up to 3 bar. Fabrics requiring such testing have reduced porosity, leading to low air permeability, and hence the use of standard air permeability testers is impractical.
- A study of the structure-property relation of nonwoven fabrics for use in gas filtration.
- A study of woven fabric structures made from twisted, untwisted and monofilament yarns and used in a wide range of applications, including various industrial filtration, breathable garment outer-layers and side/roof-deployment air bags.

Air permeability measuring instrument

Rationale:

Most woven fabrics such as those used for apparel, domestic and light industrial application are of relatively open construction. Measuring the air permeability of such fabrics can be carried out at low pressure differences and a number of instruments are available for the purpose. In contrast, some materials such as leather, certain types of coated fabrics, and fabrics created for operating at increased pressure levels necessitate measuring their air permeability at appropriately high pressure levels that standard instruments are not able to provide. An instrument capable of testing up to 300 kPa was designed and built to address this need.

Method:

An approach analogous to that employed in electrical technology for measuring high resistance values was used, where a pre-charged capacitor is discharged through a resistor and the rate of decrease in current flow determined for calculating the resistance. Similarly in this instrument, a tank of sufficient capacity, pre-charged to a suitable pressure level is used to supply air to a fabric sample. As the air leaks through the fabric, the pressure in the tank drops. Measurement of the **rate** of drop in pressure in the tank enables calculation of the airflow rate through the fabric at a given pressure.

Fabrics that are appropriate for measurement by this technique have generally reduced air permeability on account of their tighter structures or other processes to which they are subjected and make the use of standard flow measuring instrumentation difficult to use. Figure 1 shows the basic construction of the instrument. The tank T is supplied with filtered dry air through a filter/drier F and electrically controlled pressure regulator R. Solenoid valve V1 is used to stop the airflow into the tank once the tank is charged to the required pressure.

The pressure in the tank can be varied between 0.05 bar (gauge) to 3 bar. The tank can be connected to the test area through the pilot controlled solenoid valve V2 comprising of the lower clamp C1 and the upper (movable) clamp C2. Clamp C2 is controlled by an electric linear actuator so as to produce the required level of clamping force. A high response pressure transducer G1 is connected to the lower test clamp to enable the measurement of the air pressure applied to the fabric. Valve V2 has a large port area, in order for pressure loss across to be rendered negligible so that when V2 is open the reading of G1 is also very closely the pressure in the tank. There is also a low pressure transducer G2 (not shown) connected to the lower clamp. G2 is actually connected through a separate solenoid valve, so that when high pressure testing is carried out, it is isolated from the test area. G2 is provided in order that low pressure testing of fabrics can also be carried out on the same instrument. The tank can be flushed clean of any condensate using drain valve D. The pressure transducers are interfaced to a PC to enable logging of pressure data during testing. An optical proximity sensor P attached to the upper clamp to enable the measurement of distension of fabrics under pressure. The sensor employed is based on a linear optical array.

In the current configuration the test pressure can be up to 300 kPa. The test area is 50 cm². The optical proximity sensor can measure the distension of the specimen during testing.

Testing can be carried out in two ways. The tank can be pre-charged to the required test pressure, and the pressure can be applied to the fabric suddenly, with data acquisition started a few moments before. It is also possible to first connect the test area to the tank, then charge the cylinder up to the test pressure before the data acquisition is started. For the majority of fabrics tested so far, and for relatively low pressure levels, the method of pressure application makes no measurable difference.

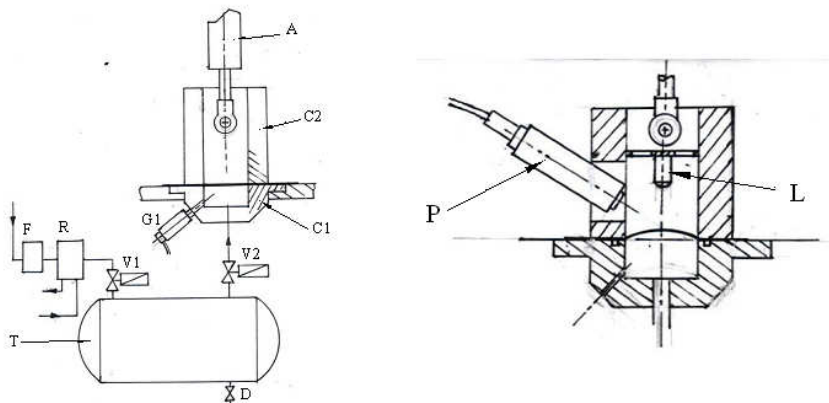


Figure 1: Basic construction of the tester

Figure 2 is a typical pressure vs. time graph obtained for a nylon-66 fabric of close woven construction.

Results and Conclusions

The graphs as obtained have a stepped nature due to digitising by the data acquisition system. They should be smoothed using a suitable technique that does not affect the gradient. Curve fitting can be applied when the pressure decay is relatively slow, as with fabrics having low porosity. Other techniques can be applied when the pressure decay is faster. Figures 2 and 3 show a p vs. t graph as obtained and the air permeability calculated as volume of free air (i.e. reduced to 100 kPa).

It can be shown that:-

$$\text{air permeability of the fabric} = (V \cdot dp/dt) / (P_{atm} \cdot A) \text{ in appropriate units,}$$

where V = effective tank volume
 dp/dt = rate of pressure decay
 A = test area
 P_{atm} = atmospheric pressure= 0.987 bar..... (1)

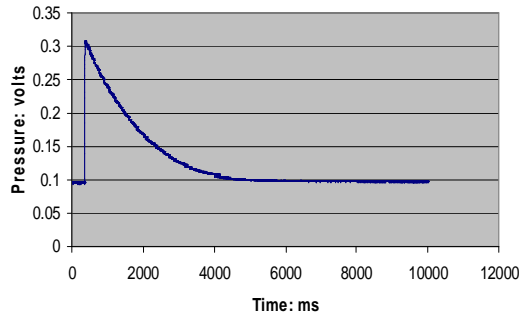


Figure 2: Pressure vs. time graph for a nylon 66 fabric

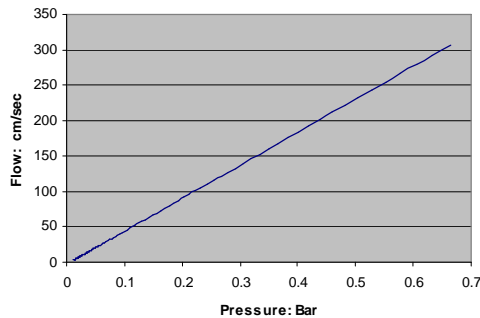


Figure 3: Calculated fabric air permeability vs. pressure

The principle of permeability measurement applied is valid even for standard fabrics which are relatively open. It was demonstrated that such fabrics can be measured by making use of the low pressure transducer (pressures up to 0.5 kPa). These fabrics require a reduction of the test area to about 5 cm², in order that the pressure decay is held to a rate that can be followed by the low pressure transducer.

Nonwoven Structure, Property and Performance for Gas filtration

Rationale:

In gas filtration processes, nonwovens are the most widely used fabrics for bag, panel and cartridge type filter media. There are three parameters that may be used to evaluate a filter media performance: filtration efficiency (E%), pressure drop (P_d) across the filter media, and the disposition towards effective cleaning at the end of each filtration cycle, i.e. the cleaning efficiency (CE) for cleanable filters. The measured values for these parameters are, inter alia, dependent on the filter structure. Fibre parameters, such as fibre type, fibre fineness, cross-sectional shape, and fabric parameters, such as mass per unit area (basis weight), fibre packing fraction, thickness, and surface characteristics, play a major part in determining the filter media structure and related properties, in particular pore size distribution, and air permeability. Although much research on the material type and properties of nonwoven filter media has been reported, no detailed comparative study has been made of the performance of the various surface treatments in respect of the structure-property relation, which is the objective of this work.

Method:

The work involved eighteen commercially available products used in bag filtration. See Table I. They included one microporous coated, one laminated expanded-PTFE, four heat-calendered, nine surface singed, and three untreated. The fibre types were polypropylene (PP), polyester (PET), aramid (AR) and nylon (PA) with fibre finenesses from 1.7 to 15 denier.

The test rig constructed for the work simulated the filter bag process and gave good reproducible results. See Fig. 4.

- Porosities, ϵ , were calculated as the percentage void volume of the structures, based on the packing densities, δ .
- The surface and internal pore structures were examined by means of a scanning electron microscope (SEM). See Fig.5 (examples of surface structures for Groups A, B and C.)
- The bubble point test was used to measure equivalent pore size, Ω , i.e. the average circular pore diameter in the filter media.
- The test results were compared with values obtained from the Wrotnowski model and the Hagen-Poiseuille law.
- The Shirley Air permeability tester was used to measure the volumetric flow rates per unit area. The values obtained were compared with theoretical estimates based on the Kozeny-Carman, Happel, Kuwabara models.
- Filtration performance of each sample was determined from the pressure drop with filtration time, the filtration cycle time for a pressure drop of 1000Pa, the filtration efficiency and the particle concentration in the gas emission.

Table I. Specifications of the Needed Nonwoven Filter Media

Sample Code (Group)	Fibre Type	Fibre Fineness F_f (Denier*)	Fibre Density ρ_f $\times 10^6$ (gm^{-3})	Fibre Dia. D_f (μm)	Basis weight W (gm^{-2})	Thickness T $\times 10^{-3}$ (m)	Porosity ϵ (%)	Surface Treatment
A1	PET	2.2	1.38	15.1	592	2.41	82	MP-C
A2	PET	2.2	1.38	15.1	572	2.07	80	PTFE-M
B1	PP	2.1	0.91	18.8	505	2.30	76	Calendered
B2	PET	2.2	1.38	14.2	500	1.68	78	Calendered
B3	PET	1.7	1.38	13.1	506	1.90	81	Calendered
B4	AR	2.0	1.38	14.3	518	2.04	82	Calendered
C1	PET	2.2	1.38	15.1	567	2.10	80	Singed
C2	PET	2.2	1.38	15.1	495	1.88	82	Singed
C3	PET	2.2	1.38	15.1	408	1.60	81	Singed
C4	PET	1.7	1.38	13.1	586	2.33	82	Singed
C5	PET	1.7	1.38	13.1	418	1.80	83	Singed
C6	PET	1.7	1.38	13.1	365	1.62	84	Singed
C7	PET	2.2	1.38	15.1	358	1.72	85	Singed
C8	PET	2.2	1.38	15.7	514	2.40	85	Singed
C9	AR	2.2	1.38	15.7	509	2.70	86	Singed
D1	PET	5.3	1.38	23.5	435	4.99	93	NO
D2	NY/PET	3.3/5.3	1.21/.38	15/22	254	3.50	94	NO
D3	PET	15.3	1.38	37	380	5.20	95	NO

W –basis weight; T – thickness; ϵ – porosity, Gr – Grouping: (PTFE-M) PTFE membrane; (MP-C) Micro-porous coating; NO – no surface treatment. * = g per

Results and Conclusions

- **Geometrical Parameters and Micro Structural Characteristics**
 - Surface finishing treatments increased packing density, particularly near the filtration surface.

The porosities of the surface treated materials varied from 76% to 86%, but Groups A and B were generally lower than Group C, which may be attributed to differences in compression effects of the surface treatment processes. The Group D materials had porosities of the order

of 94%. Generally, these materials have smooth surfaces and a higher degree of fibre packing to a depth of approximately 100µm from the surface (see Fig.6), compared with the remaining thickness of their cross-sections. In contrast, the Group D materials (not shown) had hairy surfaces and no apparent change in fibre packing density through the fabric thickness, which corresponds with having larger porosity values.

ii) There is a non linear relationship between mean pore size and fibre packing density or porosity. See Fig 6. Mean pore size is dependent on the type of surface treatment.

The micro-porous coating gives the smallest values, but the comparative differences between the micro-porous, the laminated expanded -PTFE and the heat-calendered materials were small. The pore sizes of the singed materials were much smaller than the untreated material. The Hagen-Poiseuille's and Wrontnowski's equations can be used to calculate estimates of pore size. However, the effective pore diameter (See equation 2), derived as an alternative to the Wrontnowski's circular pore diameter (See equation 3) generally gave a closer fit to the bubble point test values.

$$D_e = \sqrt{\frac{D_f^2}{1 - \varepsilon}} \dots\dots\dots (2)$$

$$D_{wp} = \left[14.87 \sqrt{\frac{F_f}{\rho_f}} \right] - D_f \dots\dots\dots (3)$$

D_e - effective pore diameter, which is the diameter of a capillary equivalent in cross-sectional area of the free space,

D_{wp} - Wrontnowski's circular pore diameter,

D_f - fibre diameter

F_f - fibre fineness (denier)

• **Specific Permeability**

iii) The relation between mean pore size and specific permeability follows a second order polynomial. See Fig.7

The coated and laminated materials had low permeability values, followed by the calendered and singed fabrics; the untreated fabrics showed much higher permeabilities. The Kozeny-Carmen, Happel and Kuwabara models did not give good estimates of the specific permeability for test specimens. A much closer fit with experimental values was achieved by using the effective pore diameter for deriving the hydraulic radius as a substitute for the flow-average pore diameter in the Hagen-Poiseuille equation.

• **Filtration Performance**

iv). Pressure drop with filtration time follows a linear rate of increase for surface treated materials, indicating a surface filtration mechanism; the gradient for the singed treated materials was almost half that for the other treated fabrics. (See Fig.8) The graph for the untreated nonwovens had a concave profile, indicative of depth filtration. The SEM observations of tested fabrics support these findings.

Whereas trapped particles were identified throughout the thickness of the untreated fabrics, none was evident for the coated, laminated or calendered media. With the singed media, particle penetration only occurred in the upper half of the fabrics, suggesting an initial depth filtration followed by surface filtration. Contrary to other reported findings, the SEM micrographs revealed no evidence of preferential trapping in the needled regions of the fabric structures.

v) The dust holding capacity of the filters and the particle concentration in the post filter airflow (See Figs 9 & 10) were distinctly lower for the coated and calendered products; these also gave the higher values of filtration efficiency. See Fig.11.

vi). Contrary to other reported findings the base fabric appeared to have a significant influence on cake formation and cake permeability.

Differences in the airflow resistance of the filter cake formed on the treated fabrics indicated the likely effect of the structural characteristics of a filter fabric on surface filtration. Essentially, the cake resistance increases with reduced fabric air permeability. It is reasoned that at the early stages of cake formation a closer packing of dust particles occurs on lower permeable surfaces, since particle penetration into and through the fabric would be small. This results in higher filter cake resistance.

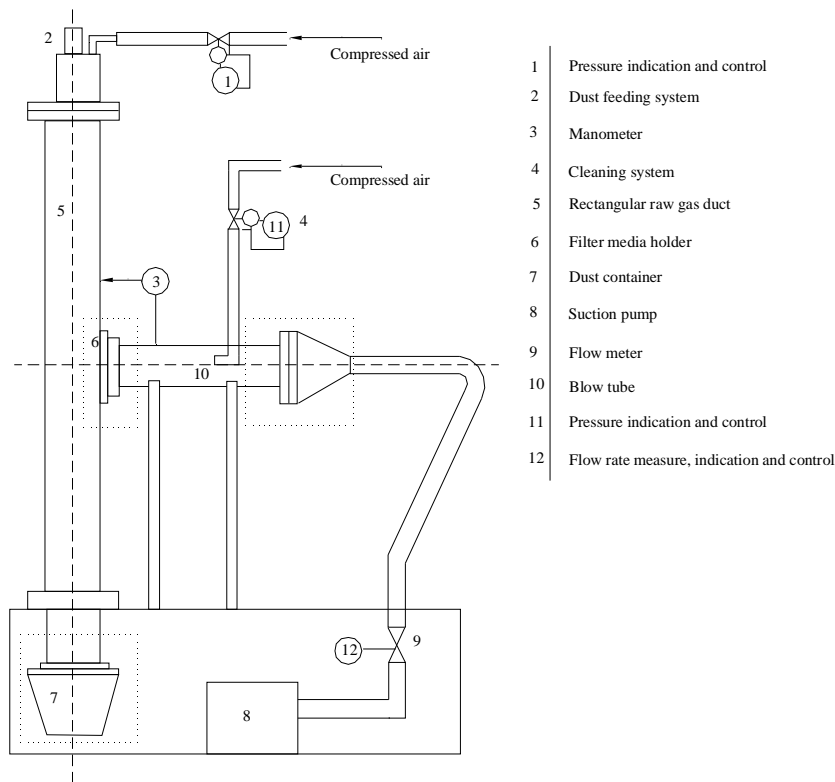


Fig.4 Filtration Test Apparatus

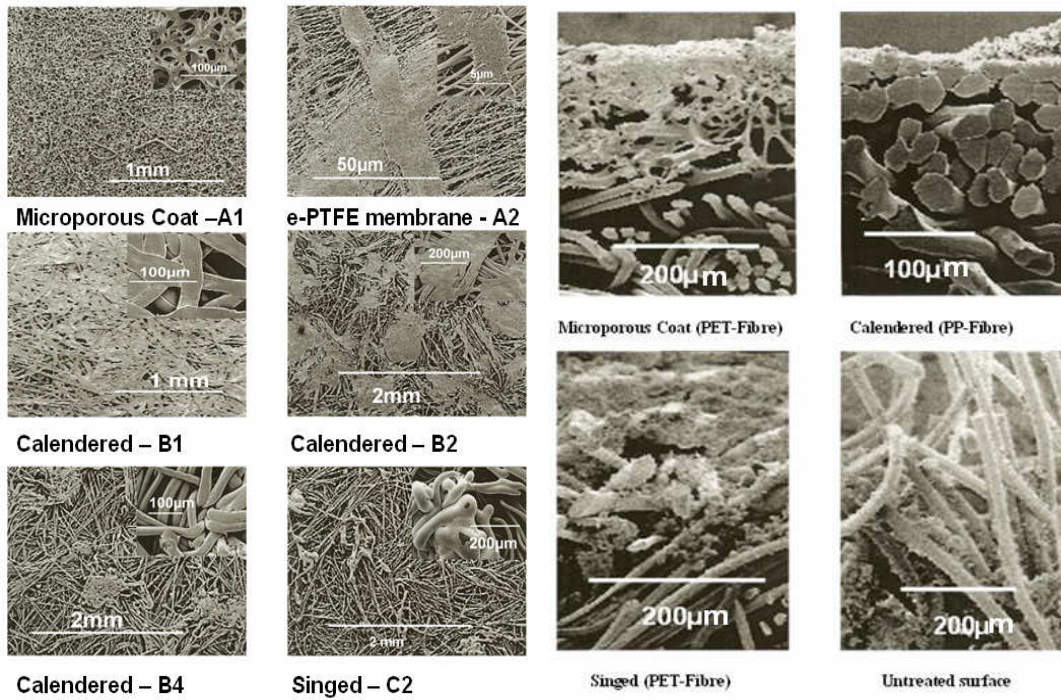


Fig.5 SEM Micrographs of Surface Treat Fabrics

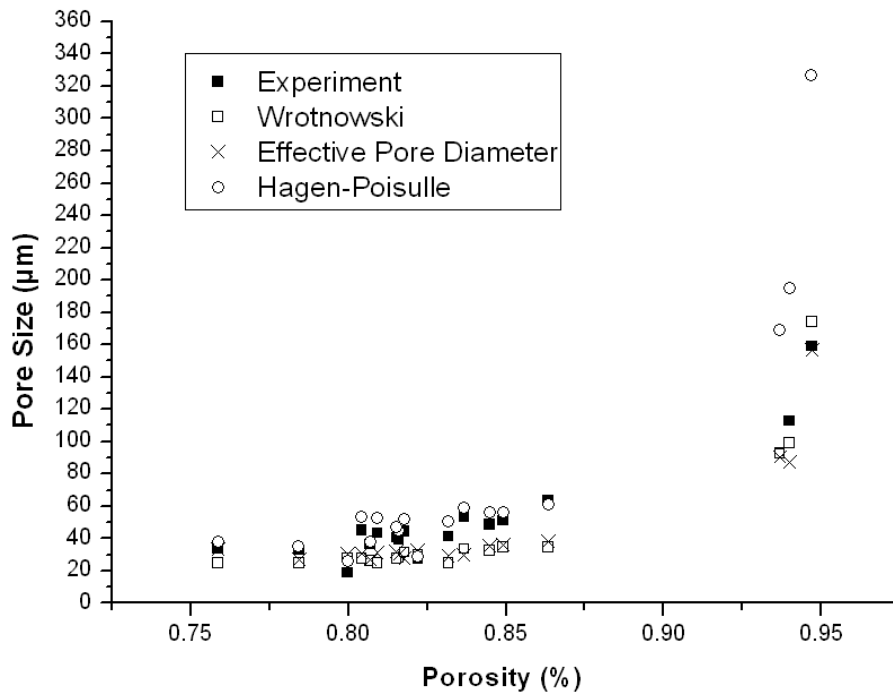


Fig.6 Pore Size vs. Porosity

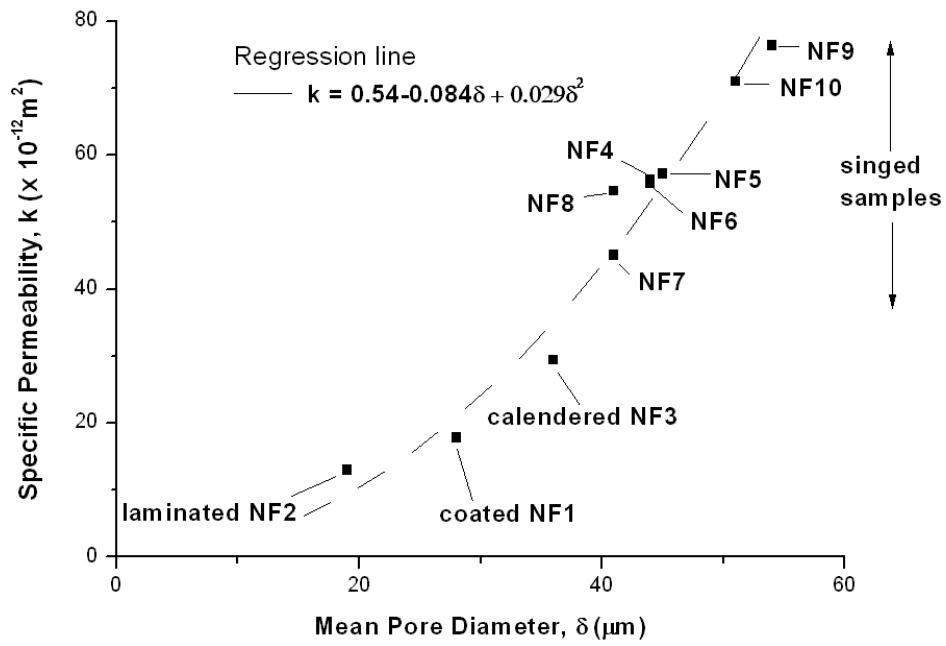


Fig.7 Specific Permeability vs. Mean Pore Diameter

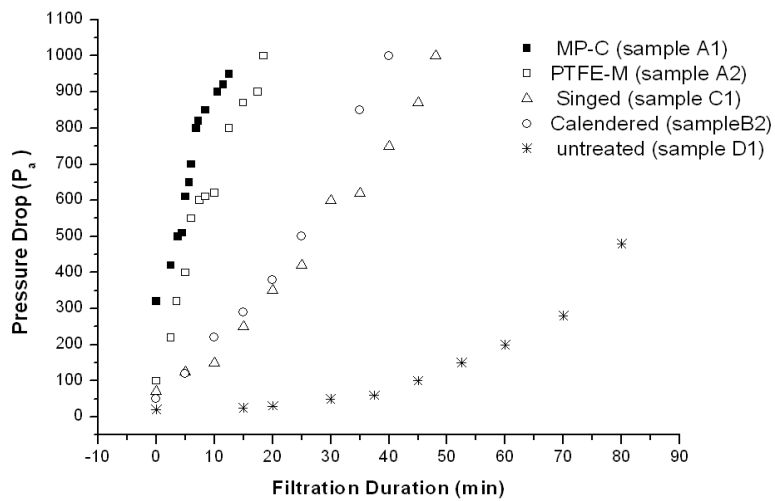


Fig.8 Pressure Drop with Filtration Time

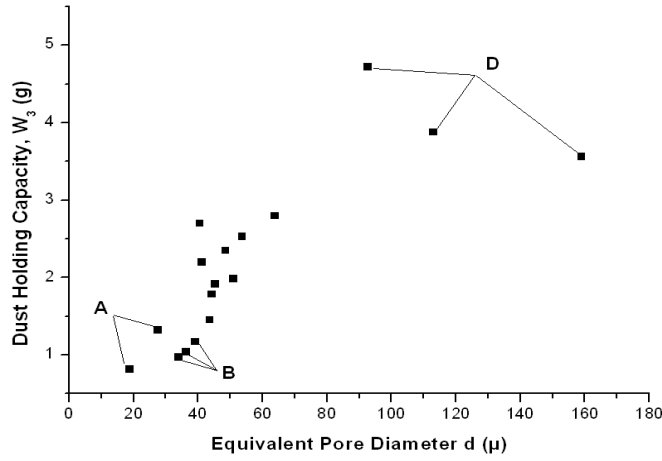


Fig.9 Effect of Pore Size on Dust Cake Mass

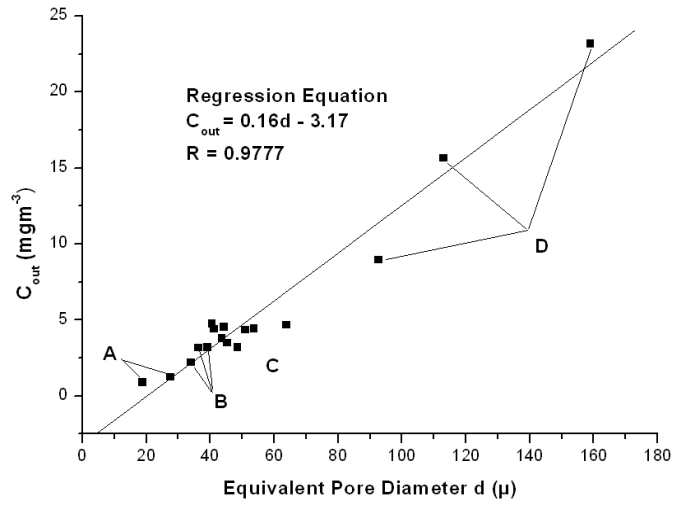


Fig.10 Relationship between Pore Diameter and Exhaust Particles

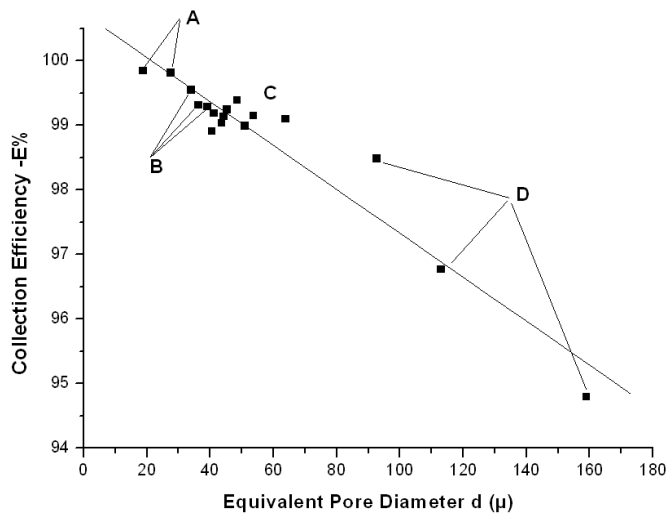


Fig.11 Effect of Pore Size on Filtration Efficiency

Permeability of Plain Weave Filament Fabrics

Rationale

The work carried out investigated three things.

1. Firstly, to determine if the trend of airflow velocity through a narrow orifice under increasing pressure drop is similar to the flow through a wide range of very different plain weave fabric constructions made from filament yarns. The association of fabric permeability and porosity is complex. For example, in terms of the fabric interstices, the fabric's permeability may be considered in respect of three factors; a) cross-sectional area of the pores, b) the height of pores; this is proportional to the fabric thickness, T, and c) number of pore per unit area. However, fibre fineness and its cross-sectional shape affects the flow rate due to the surface area and air space between fibres, determined by the packing fraction of fibres in a yarn and fibres of different cross-sections will pack together differently. The type finish given to a fabric can have a considerable effect on the fabric permeability even though the porosity may remain the same.

Although the shape and size of pores cannot be defined with accuracy, the trend of fabric permeability with pressure drop can be obtained by considering the airflow through a pore simulated by airflow through a cylindrical hole of known diameter and length. Hoerner [S. F. Hoerner, "Aerodynamic properties of screen and fabrics", *Textile Research Journal*, 1952, April, P274] used wire mesh for his model, and assumed that the wire mesh and a screen fabric both behave similarly under the same conditions and argues that pressure drop is due to the friction between the air and the contact surface area of the medium as well as the speed of flow. He suggests that the airflow through a fabric is similar to the airflow through a tube, but with the effect of a greater aspect ratio. Robertson [A. F., Robertson, "Air porosity of open weave fabrics: Part I: Metallic meshes" *Textile Research Journal*, 1950, December, P838] also considered a wire mesh as a simplified model of a fabric and each pore space between cross-overs of warp and weft to be a nozzle with equal discharge coefficient.

2. Secondly, based on findings from the above work, to establish a general model that could be used for predicting the air permeability of plain weave filament cloths.

Previous studies reported in the literature were concerned with staple spun yarns, and the airflow through fabric made from staple yarns is very different from fabrics constructed from filament. However, Saidenov [Saidenov 1964] suggested the following two term equation for the prediction of fabric air permeability under a pressure drop of Δp , (Pa).

$$\Delta p = aU + bU^2 \dots\dots\dots (4)$$

The constants a, and b are related to the fabric cover factor K, i.e. the fraction of unit area of fabric surface occupied by the constituent fibres/yarns. This equation shows that for a given fabric structure, U may be linearly related to Δp , when $b \rightarrow 0$, $K \rightarrow 1$; or increase non-linearly with Δp , when $a \rightarrow 0$, $K \ll 1$. If the flow through the interstices of a plain weave fabric from filament yarns shows a similar trend to through a narrow orifice, then it is of interest to establish which part of the Saidenov's expression may be the dominant factor.

3. Thirdly, to determine if with x-ray tomographic data for 3D structural geometry of fabrics, numerical techniques such as Lattice Boltzmann Method (LBM) could be used to give useful information on the airflow through woven structures.

X-ray microtomography (XMT) operates on the same basic principles of a hospital CT scanner, but with much higher power and spatial resolution. As the name suggests, typical spatial resolution of XMT is in microns, as opposed to millimetres for medical CT scanners. Some commercially available desktop XMT equipment is only a fraction in size, weight and cost of medical CT scanners. The enhanced spatial resolution, portability and affordability, and the non-destructive nature of the measurement technique, are making XMT an

increasingly popular means for scientists and engineers to characterise structures of various materials in full 3D with unprecedented level of details.

The LBM may be regarded a 'digital' equivalent of the convectional continuum based computational fluid dynamics (CFD). It is performed on a regular – usually cubic – lattice grid and the calculations are local to each grid cell. The lattice approach and data localisation make it easy to deal with arbitrary geometries, hence its appeal as a numerical technique for calculating flow through porous media. While a full treatment of the subject can be found in the literature elsewhere (Succi 2001), only the basic principles are presented here. The LBM maps physical space onto a regular lattice grid and all the calculations are performed on the grid cells (also called nodes or sites). Associated with each node is a set of mass probability distributions, also referred to as particle distribution functions or simply density. These distributions propagate to neighbouring nodes, as part of mass and momentum transfer, along fixed velocity vectors at each time step, followed by simple collisions designed to conserve mass and momentum. The collision operator is chosen such that the particle velocity distributions at each node obey the Navier-Stokes equations in the low Knudsen number and low Mach number regime:

$$\frac{1}{c_s^2 \rho_0} \frac{\partial p}{\partial t} + \nabla \cdot \vec{u} = 0 \quad (5)$$

$$\frac{\partial \vec{u}}{\partial t} + \vec{u} \cdot \nabla \vec{u} = -\frac{\nabla p}{\rho_0} + \nu \nabla^2 \vec{u} + \vec{f}$$

where c_s is the speed of sound, ρ_0 the mass density of the fluid, p the hydrodynamic pressure, \vec{u} the fluid velocity, ν the kinematic viscosity, and \vec{f} an external body force. In the LBM, the evolution of the particle distribution functions f_i is described as:

$$f_i(\vec{x} + \vec{e}_i, t + 1) = f_i(\vec{x}, t) - \frac{1}{\tau} [f_i(\vec{x}, t) - f_i^{eq}(\vec{x}, t)] \quad (6)$$

where \vec{x} is the (x,y,z) coordinates of node i , \vec{e}_i the i -th component of the velocity vector, t the time, f_i^{eq} the equilibrium distribution, and τ a relaxation parameter. The left hand side of the equation describes the propagation or translation, whereas the right hand side the collision operation in which all the instantaneous distribution functions relax at a single rate to their equilibrium values. The time step in a LBM simulation is customarily set to 1, so is the magnitude of the velocity components. As such, everything else (e.g. length scales, velocities and pressure) is in lattice units. The D3Q19 scheme is adopted for this work, which operates on a 3D cubic lattice grid with each grid cell interacting with 18 (out of 26) of its closest neighbours. There are 19 velocity components in the velocity vector for each node, and the equilibrium distributions were chosen as:

$$f_0^{eq} = \frac{\rho}{3} \left[1 - \frac{3}{2} u^2 \right] \quad (7)$$

for the zero velocity component,

$$f_i^{eq} = \frac{\rho}{18} \left[1 - 3(\vec{e}_i \cdot \vec{u}) + \frac{9}{2} (\vec{e}_i \cdot \vec{u})^2 - \frac{3}{2} u^2 \right] \quad (8)$$

for the 6 orthogonal velocity components, and

$$f_i^{eq} = \frac{\rho}{36} \left[1 - 3(\vec{e}_i \cdot \vec{u}) + \frac{9}{2} (\vec{e}_i \cdot \vec{u})^2 - \frac{3}{2} u^2 \right] \quad (9)$$

for the 12 diagonal velocity components.

With these equilibrium functions, it can be shown that Equation (2.3) is equivalent to the Navier-Stokes equation, Equation (2.1), with all the terms now being dimensionless:

$$\frac{d\bar{u}'}{dt} = -\frac{1}{\rho'} \nabla p' + \nu' \nabla^2 \bar{u}' \quad (10)$$

where

$$\bar{u}' = \frac{\bar{u}}{\sqrt{3}c_s} \quad 3p' = \rho' = \sum_i f_i \quad \rho' \bar{u}' = \sum_i f_i \bar{e}_i + \tau \rho' \vec{f}' \quad \nu' = \frac{2\tau - 1}{6} \quad \vec{f}' = \frac{\vec{f}}{\rho_0} \quad (11)$$

To estimate the intrinsic permeability of a porous structure, as defined by the Darcy's law, the following formula is used:

$$k' = \frac{\bar{u}' \nu'}{f'} \quad (12)$$

where \bar{u}' is the superficial or Darcy velocity which is a mean fluid velocity averaged over a cross-section (including the solids) normal to the direction of the flow. ν' is related to the relaxation parameter τ by Equation (7) and f' the body force. Both τ and f' are user definable input. \bar{u}' is a simulation output. Permeability k' estimated using Equation (8) is in lattice units lu^2 where lu is the unit length scale in LBM (customarily set to 1). Since the LBM simulations, the structures used were obtained using X-ray tomography without rescaling, lu is equal to the pixel resolution of the scanned structure. To convert the k' value from lattice units to physical units, k' is multiplied by the square of pixel width, w_p :

$$k = k' \times w_p^2 \quad (13)$$

Method:

Eight commercially available plain weave fabrics and fifteen in-house produced fabrics all of different constructions, and woven from filament yarns were used for the work. Fig.11 shows photomicrographs of three fabric structures to illustrate the wide variation of fabrics considered. Essentially, fabrics were made from twisted filaments, untwisted filaments and monofilaments. The number of filaments in the yarns, and the counts of the filaments and of the yarns were varied. The air permeabilities of these fabrics were measured for increasing pressure drop. Owing to the wide differences in the void dimensions of the fabrics, the test area of the permeability instrument constructed had to be varied in order that the airflow rates for a given range of pressures could be kept within the measurable range of the instrument. Several inserts were made to reduce the test area from 5.07 to the following sizes: 2, 1.5, and 0.25cm².

The trends of airflow rate, Q , through orifices of different dimensions (diameters ranging from 0.5 to 2mm, length 0.7 to 22mm, inclination from vertical to 45°) and combination of sizes were determined and compared with experimental data for the above fabrics.

A SkyScan 1072 XMT unit was used for the work. A reconstructed image (also known as a tomogram) is a cross-sectional slice of the object, parallel to the X-ray – assuming the X-ray is an idealised fan-shaped beam. By stacking the slices, a full 3D digital structure is obtained, which can then be digitally sectioned to provide cross-sectional views in any direction. Figure 12a shows an example of X-ray shadow images – the so-called projections – from which the slices or tomograms are reconstructed and an example of which is given in Figure 12b. Stacking the reconstructed images, a 3D volumetric representation of the fabric was obtained.

Figure 13a shows an example after applying a threshold to distinguish voids from the fabric material.

Results and Conclusions

i) The flow rate through the orifice plates increased nonlinearly with applied pressure drop, ΔP .

As may be expected, the magnitude and rate of increase of Q with ΔP is greater for an orifice of larger diameter, shorter length and 90° inclination. The effect of diameter was greater than length and inclination, which in turn were similar to each other. Combinations followed a similar pattern to increasing size holes. However, the flow velocity is effectively the same for the differing orifices, with again the magnitude and rate of increase of Q following expectations of pore dimensions.

ii) With the fabrics shown in Fig.11, Q also increased non-linearly with ΔP ; the nonlinearity being strongest for the monofilament, followed by the twisted filament based fabric. The untwisted filament based fabric shows a tendency to linearity at ΔP values $> 10\text{mmH}_2\text{O}$. See Fig.14(A).

iii) In general, the pressure drop through the fabric may be represented by an equation of the general form

$$U = \kappa \Delta P^m \dots\dots\dots(14)$$

Where $m = 1$ and $k = k_1$ or $m = 0.5$ and $k = k_2$ and $U =$ mean flow velocity

The constants k_1 , and k_2 were found to be related to the fabric cover factor K. This equation therefore shows that for a given fabric structure, U may be linearly related to Δp , when $k_2 \rightarrow 0$, $K > 0.98$; or increase non-linearly with Δp , when $k_1 \rightarrow 0$, $K < 0.98$.

In the first instance the equation is of the form of Darcy's law, suggesting viscous type flow behaviour. In the second instance the form is typical of Bernouille's equation for non-viscous flow behaviour. Measurements of U for fabrics with K values from 0.98 to 0.99 were compared with calculated U data for viscous type flow. Similarly, measurements of U for fabrics with K values from 0.978 – 0.471 were compared with calculated figures for non-viscous type flow. The U_{cal} values were plotted against the U measured, U_{meas} . Ideally

$$U_{cal} = ZU_{meas} + L \dots\dots\dots(15)$$

Where $Z = 1$ and $L = 0$.

Generally Z ranged from 0.8 to 0.98 and $L \ll 0.05$, the correlation coefficients were $R = 0.98$ to 0.997

iv) LBM was also used to calculate the flow through the fabrics and was found to give predicted values very close to the experimental measurements.

Figure 13a) & b) shows as an example, a section of fabric SSS2 and the high flow rate zones through the fabric. Figure 13c shows a cross-sectional view of the flow field as a contour, and Figure 13d depicts the corresponding flow distribution (the flow is facing the page). As a further example Fig.14(B) shows LBM calculated U vs. ΔP for SS3 and as can be seen the values are very close to those in Fig14(A).



Fig.11 Fabric Construction

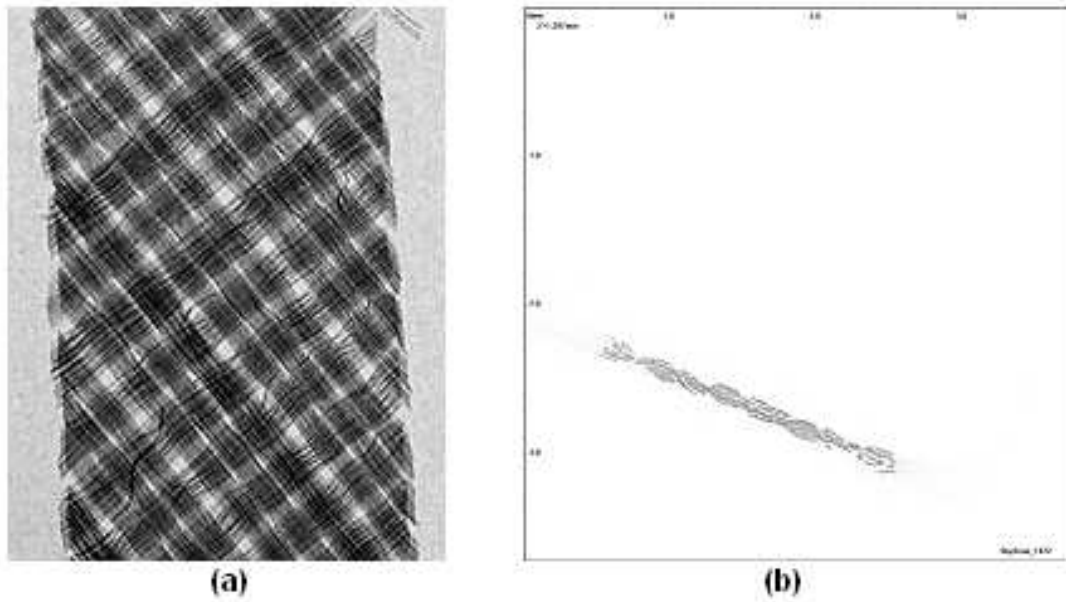


Figure 12(a) Shadow X-ray image of a SS-2 sample (after image processing to enhance the contrast). (b) A typical example of reconstructed slices, with scale annotation in mm units.

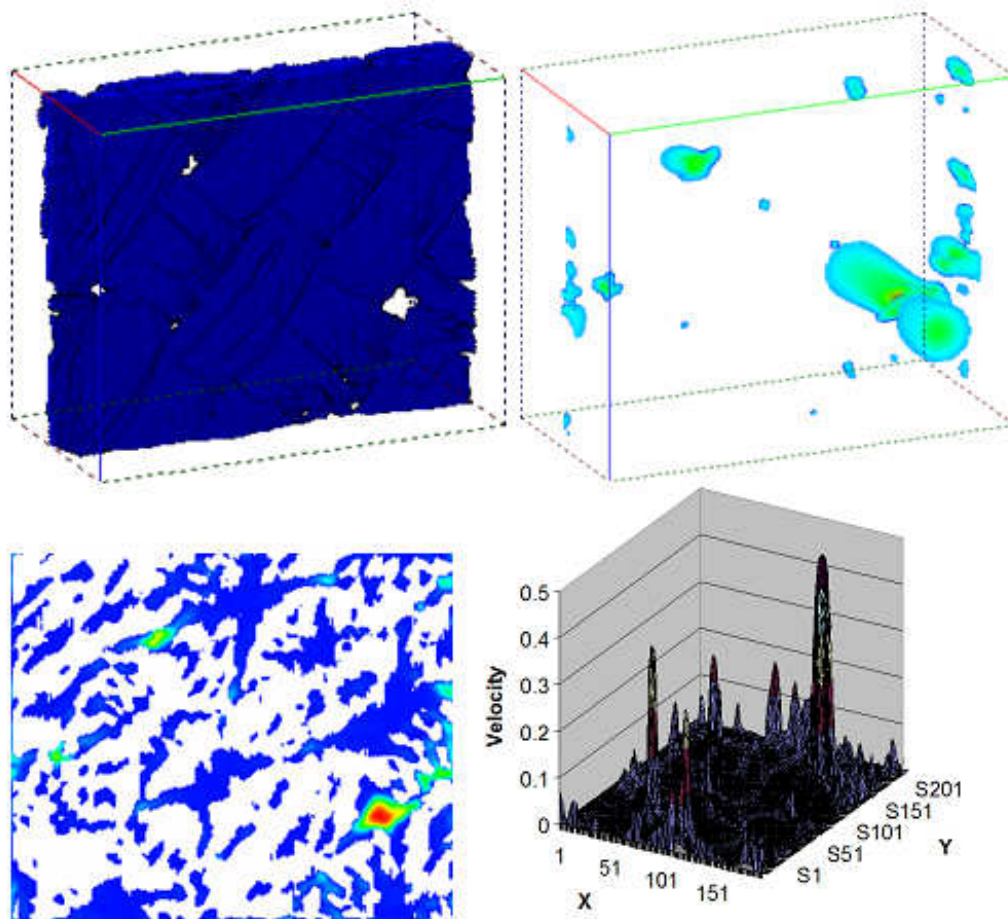


Figure 13 (a) 3D view of a cut-out section of XMT imaged SS-2 sample. (b) LBM simulated distribution of high flow-rate zones. (c) Cross-sectional view of velocity field. White pixels are fibres. (d) Surface contour plot of the velocity distribution at the same cross-section.

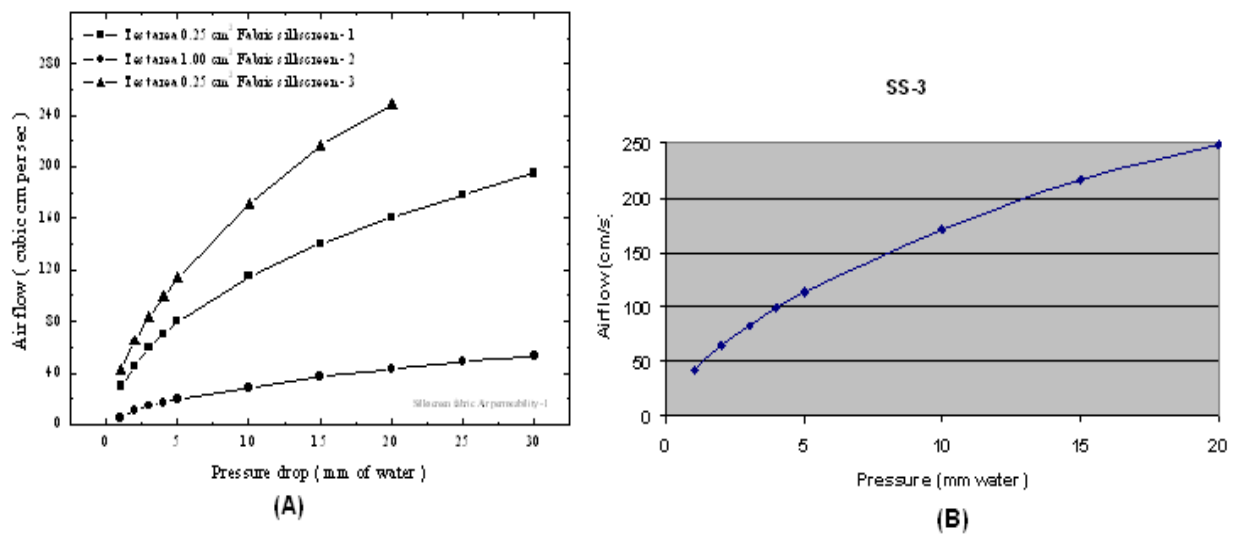


Fig.14 Airflow rate vs. pressure drop

Moisture Vapour Transfer through Breathable Fabrics

Rationale

Fabrics for waterproof breathable garments may be coated or laminated with a microporous or hydrophilic polymer, or occasionally a combination of these two technologies is used. It is believed that the transport properties of these materials depend on the temperature and humidity on both sides of the membrane surfaces. With no applied air pressure difference across the membrane thickness, transport of water vapour occurs purely by diffusion, according to Fick's Law, driven by vapour concentration differences. Current test standard methods assess water vapour transport under isothermal conditions. However, the conditions under which these materials are used in practice involve temperature and humidity gradients. It is believed that under such conditions the diffusion constant of Fick's equation becomes a function of temperature and humidity. The purpose of this study was to examine the effect of temperature and humidity gradients on the moisture vapour transport properties of waterproof breathable fabrics.

Methodology:

A modification of the BS 7209 evaporative dish method was chosen for the work, since an evaluation of the various methods showed this would enable the testing of the membrane under the more realistic conditions referred to above. This method expresses absolute moisture vapour transmission rate (MTVR) as percentage permeability of the MTVR of a tightly woven polyester reference fabric that is measured concurrently, results can also be expressed in terms of the loss of mass per unit area for a given time period.

Figure 15 illustrates the test apparatus developed. Three temperature and humidity sensors were utilised, one placed above the sample and two below (one 1mm below the fabric and the second 2 mm). It was believed that monitoring the microclimate below the fabric would allow the vapour concentration gradient to be measured and the fabrics MVT calculated, in much shorter times than is normally needed for BS 7209. Allowance was also made for heating the dishes to reflect the warm human body usually found within garments made from waterproof breathable fabrics.

Calibration of the sensor system checked in a UKAS calibrated, Weiß SB11 series climate chamber and the results showed good agreement. See Fig.16.

Results and Conclusions

i) Early tests in a controlled environment gave good results but demonstrated that small environment changes affect the test, as seen in Fig. 17 where the three sensor readings are shown for an impermeable fabric layer and chamber cycling artefacts are clear. As a result further tests were performed from a set starting point in terms of chamber conditions and the chamber was allowed to run uncontrolled throughout the experiment. Results for a commercial fabric are also shown in Fig.17 where the Relative Humidity difference between the two sensors under the fabric is depicted. It can be seen that this difference quickly becomes constant.

Further work needs to be done to relate this difference to the weight loss recorded during the experiment, but it can be used currently to roughly categorise fabrics as the greater this difference the greater the MVT of the fabric. It is interesting to note that even when an impermeable layer is tested the environment close to the fabric does not reach 100% RH, as some researchers have stated and some test methods assume.

ii) The moisture vapour transmission of hydrophilic polymer coatings and membranes are seriously affected by changes in the ambient conditions and the environmental conditions specified in most standard test methods will militate against these polymers when high MVT is desirable.

Results gained by varying the ambient temperature can be seen in Fig.18. They show that microporous polymers demonstrate a slight decrease in MVT as the temperature drops,

probably due to a decrease in segmental motion of the polymer chains. Hydrophilic samples are, however, affected significantly by changes in ambient temperature. When the ambient temperature was reduced to 10°C the MVT figures fell significantly, but a further decrease to 5°C resulted in a large increase in transmission figures. This is confirmed in work by other researchers and further work points to this being due to a decrease in the polymers solubility coefficient at 10°C which is offset at higher temperatures by an increase in the diffusion coefficient. Also, of more interest are the results gained by varying the ambient relative humidity whilst holding the temperature constant, examples can be seen in Fig.19. This clearly shows that for hydrophilic materials the moisture vapour transmission is a function of the average relative humidity and that these polymer films do not obey Fick's Law.

iv). Attempts at mathematically modelling non-fickian diffusion from first principles have so far failed; the main problem is in defining the diffusion and sorption coefficients. However, test results have shown that all the hydrophilic compositions assessed exhibit the same linear change in MVT as the ambient relative humidity changes and this has allowed a simple predictive model to be developed which now needs to be related to performance in realistic conditions up to and including precipitation.

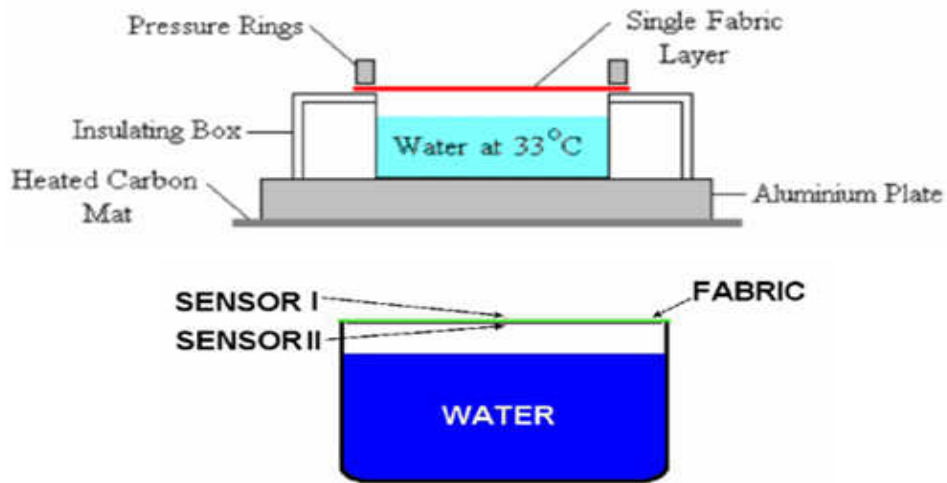


Figure 15. Proposed test method.

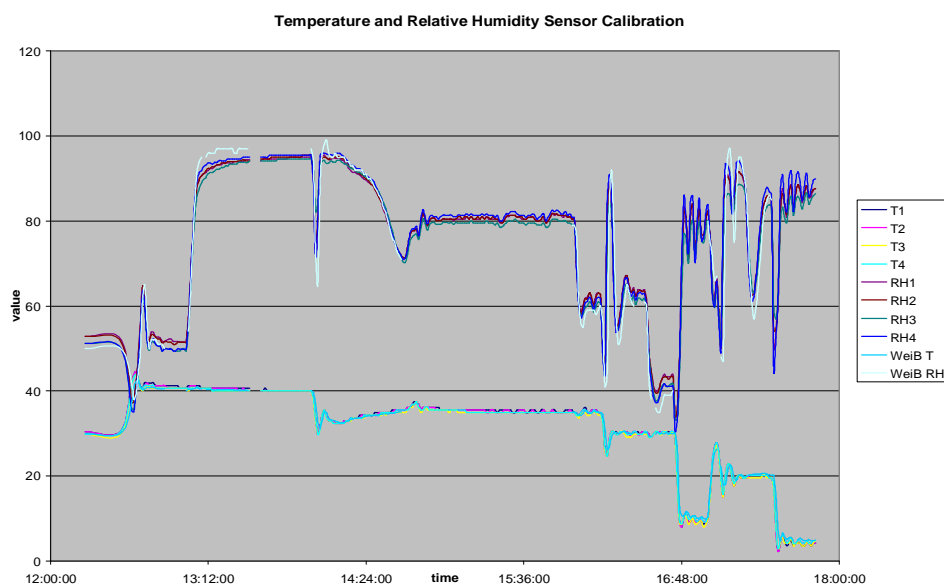


Figure 16 Calibration.

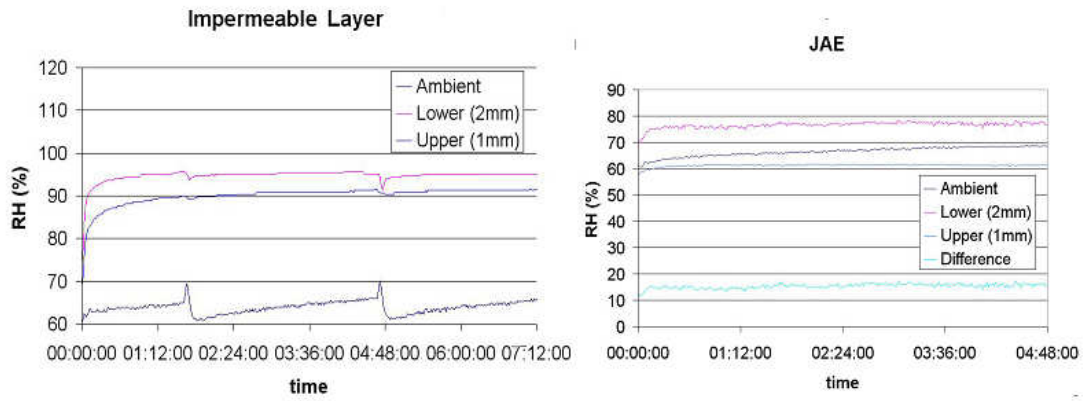


Fig.17 Sample test results

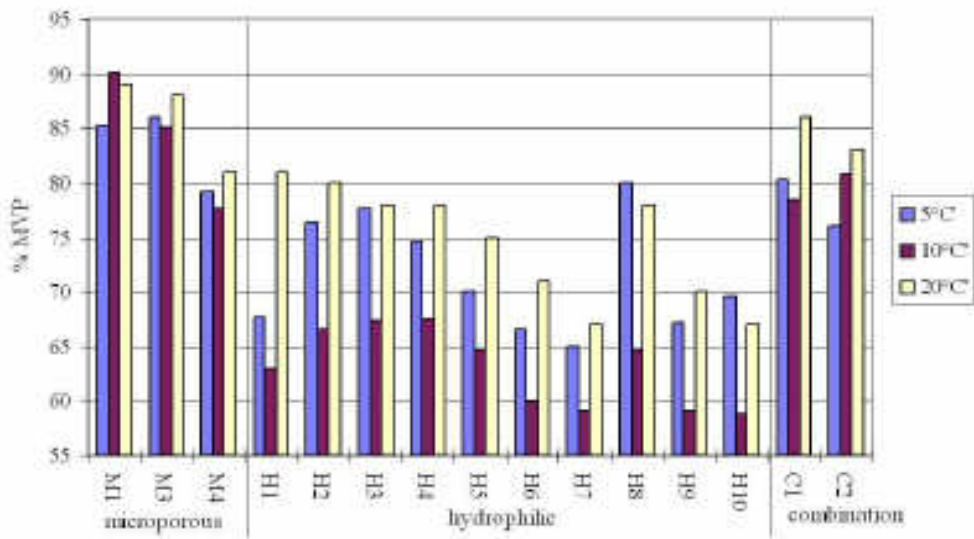


Fig.18 Test Results

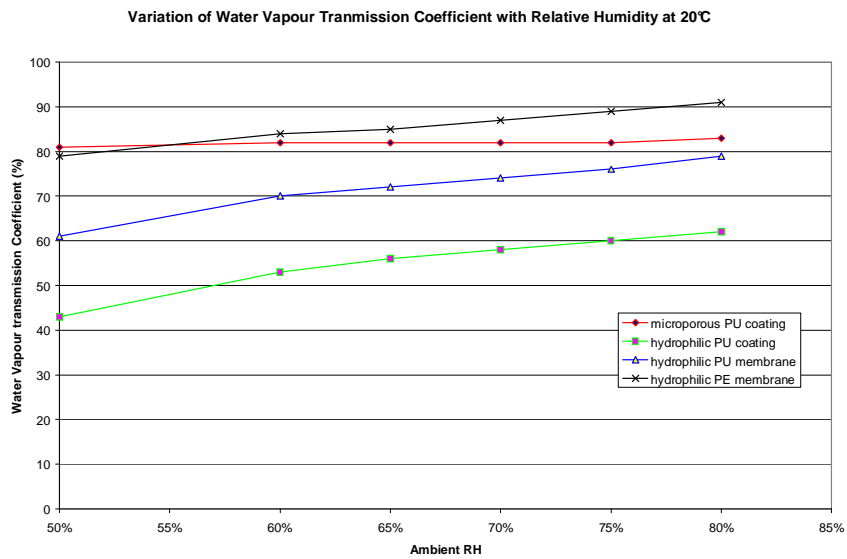


Fig.19 Test Results